

Theory of polarization-averaged core-level molecular-frame photoelectron angular distributions: I. A Full-potential method and its application to dissociating carbon monoxide dication

F Ota¹, K Yamazaki^{2,‡}, D Sébilleau³, K Ueda⁴ and K Hatada⁵

¹ Graduate School of Science and Engineering for Education, University of Toyama, Gofuku 3190, Toyama 930-8555, Japan

² Institute for Materials Research, Tohoku University, 2-1-1 Katahira, Aoba-ku, Sendai 980-8577, Japan

³ Département Matériaux Nanosciences, Institut de Physique de Rennes, UMR UR1-CNRS 6251, Université de Rennes, F-35000 Rennes, France

⁴ Institute of Multidisciplinary Research for Advanced Materials, Tohoku University, Katahira 2-1-1, Aoba-ku, Sendai 980-8577, Japan

⁵ Faculty of Science, Academic Assembly, University of Toyama, Gofuku 3190, Toyama 930-8555, Japan

E-mail: hatada@sci.u-toyama.ac.jp

Abstract. We present a theoretical study of the polarization-averaged molecular-frame photoelectron angular distributions (PA-MFPADs) emitted from the $1s$ orbital of oxygen atoms of dissociating dicationic carbon monoxide CO^{2+} . Due to the polarization-average, the contribution of the direct wave of the photoelectron which represents the largest contribution to the MFPADs is removed, so that the PA-MFPADs clearly show the details of the scattering image of the photoelectron. As a result, it is necessary to employ an accurate theory for the theoretical analysis of the continuum state. In this study, we apply a Full-potential Multiple Scattering theory, where the space is partitioned into Voronoi polyhedra and truncated spheres, in order to take into account the electron charge density outside the physical atomic spheres. We do not use the spherical harmonics expansion of the cell shape functions to avoid divergence problems. The potentials in the scattering cells are computed using the Multiconfigurational Second-Order Perturbation Theory Restricted Active Space (RASPT2) method in order to take into account the influence of the core hole in the electron charge density in the final state, so that to a realistic relaxation can be achieved. We show that the Full-potential treatment plays an important role in the PA-MFPADs at a photoelectron kinetic energy of 100 eV. By contrast, the PA-MFPADs are not sensitive to any type of major excited states in the Auger final state. We also study the dynamics of the CO^{2+} dissociation. We find that the PA-MFPADs dramatically change their shape as a function of the C-O bond length.

Keywords: PA-MFPADs, Multiples Scattering theory, Full-potential, FEL

Submitted to: *J. Phys. B: At. Mol. Opt. Phys.*

‡ Present address: Attosecond Science Research Team, Extreme Photonics Research Group, RIKEN Center for Advanced Photonics, RIKEN, 2-1 Hirosawa, Wako, Saitama, 351-0198, Japan.

1. Introduction

Core-level photoelectron diffraction (PED) is a well-known technique to probe surface structure [1]. In order to apply PED to gas-phase molecules, the molecule must be fixed in space. Experimentally, this can be realized by angle-resolved coincidence measurements between core-level photoelectrons and fragment ions [2]. With the advent of position sensitive detectors [3] and COLTRIMS-Reaction Microscope [4], the measure of momentum correlations between core-level photoelectrons and fragment ions to extract the photoelectron angular distributions in the molecular frame has become a standard approach to study molecular photoionization, see, e.g. the first paper on MFPADs measured by this technique [5].

From a theoretical point of view, it is rather straightforward to calculate MFPADs with the codes available for molecular photoionization studies. For the theoretical tools for molecular photoionization studies in general, see, e.g., [6, 7]. One of the widely used approach to calculate MFPADs is to use relaxed-core Hartree-Fock (HF) continuum orbitals in the final-state wavefunction [8, 9]. The continuum orbitals may be obtained by iteratively solving the Lippmann-Schwinger equation associated with the one electron Schrödinger equation with a potential produced by the transition-state orbital [10, 11]. To take account of electron correlations, Semenov *et al.* [12, 13] employed random-phase approximations, while Lucchese and collaborators employed multichannel Schwinger configuration interaction (MCSCI) methods [14, 15]. Density Functional Theory (DFT) and time-dependent DFT (TDDFT) [16] have also been used to simulate MFPADs [17, 18].

At higher photoelectron energies, say, ~ 100 eV and above, the multiple scattering method within the Muffin-tin approximation, which is a standard tool for PED from solid surfaces [19], has been employed also for calculations of the MFPADs of the gas phase molecules [20]. The multiple scattering method within the Muffin-tin approximation is a powerful tool thanks to the good convergence of the angular momentum multi-center expansion of the local numerical basis. Therefore, this method allows to treat relatively large polyatomic molecules. We find, however, that it gives a non-negligible error in the MFPADs, especially in the forward scattering directions. This is because the Muffin-tin approximation neglects the covalency and weak potential features out of the sphere which contributes to the small-angle scattering. In the present study, in order to improve the multiple scattering method beyond the Muffin-tin approximation, we introduce a recently-

developed Full-potential approach, which fills up the space with Voronoi polyhedra and truncated spherical cells. This allows to take into account the electron charge density outside the physical atomic cells of the target molecule. Note that the cell shape function is not expanded into spherical harmonics to avoid convergence problem. This approach has been successfully applied to X-ray Absorption Near Edge Structure (XANES), and has led to substantial improvements for low dimensional systems which have a strong anisotropy [21, 22, 23]. These improvements over Muffin-tin calculations were observed in particular in the low energy region (about 50 eV from the edge). In the higher energy region, $\gtrsim 100$ eV, there was no noticeable difference observed between the Muffin-tin and the Full-potential XANES calculations.

It should be noted that the MFPADs depend on both the molecular axis and the direction of polarization of the ionizing radiation. Recently, it was noticed that the molecular structural information is captured in the polarization-averaged MFPADs (PA-MFPADs). Due to the polarization-averaging, the contribution of the direct wave of the photoelectron, which is the largest contribution to the MFPADs, is removed so that the PA-MFPADs clearly show the scattering image of the photoelectron. Williams *et al.* [24] were the first to demonstrate that PA-MFPADs capture the directions of the bonds in polyatomic molecules (CH₄). Stimulated by this experimental work, Plésiat *et al.* [17] calculated the PA-MFPADs for many different molecules in a wide range of photoelectron energies, using DFT. Fukuzawa *et al.* [25], on the other hand, demonstrated that one can extract the bond length of the symmetric linear molecule (CO₂) from the PA-MFPADs.

The advent of XFEL [26] has stimulated a new surge of interest in the study of MFPADs since time-resolved MFPADs or PA-MFPADs using XFEL pulses as ionizing pulses may open a new pathway to make molecular movies. Using a Plane Wave approximation at a electron kinetic energy of 1 keV, Krasniqi *et al.* [27] theoretically demonstrated that the light-induced structural changes of polyatomic molecules can be extracted from the MFPADs. Kazama *et al.* [20], on the other hand, used the multiple scattering method within the Muffin-tin approximation to demonstrate that it is possible to extract the molecular structure from experimental MFPADs recorded at electron kinetic energies of about 100 eV, thereby opening the way to time-resolved MFPADs measurements with FEL. Very recently, at the soft X-ray beam line of the European XFEL [28], the first high-repetition-rate XFEL, Kastirke *et al.* [29] have performed the first successful PA-

MFPADs measurements at electron kinetic energies of ~ 100 eV, using diatomic molecules O_2 as a sample, thereby demonstrating the feasibility of making molecular movies by using a combination of a COLTRIMS-Reaction Microscope and a high repetition rate XFEL.

In the present work, we consider the process where the first XFEL pulse produces CO^{2+} via the Auger decay that follows the core ionization of CO and then, the second XFEL pulse kicks out an oxygen $1s$ electron from CO^{2+} . In Sections 2 and 3, we derive the expressions of the PA-MFPADs for core-level photoemission within the Full-potential multiple scattering theory. The results and their discussion are given in Section 4. We demonstrate then that the PA-MFPADs are not sensitive to the electronic structure, which may differ depending on the Auger final states. Employing a particular electronic configuration of the dicationic state, we show how the PA-MFPADs evolve as a function of the internuclear distance. Finally, we compare the present results to those obtained within the more commonly used Muffin-tin approximation. This highlights the importance of a proper description of the scattering potentials.

2. Theory

2.1. Full-potential Multiple Scattering Theory

We start from the identity obtained from the Green's theorem for the free electron Green's function $G_0^+(\mathbf{r} - \mathbf{r}')$ and the solution of the Schrödinger equation $\psi^+(\mathbf{r}; k)$ for the outgoing wave boundary condition at the surface of the cluster [22]

$$\begin{aligned} & \int_{S_o} \left[G_0^+(\mathbf{r}'_o - \mathbf{r}_o; \kappa) \nabla \psi_o^+(\mathbf{r}_o; k) \right. \\ & \left. - \psi_o^+(\mathbf{r}_o; k) \nabla G_0^+(\mathbf{r}'_o - \mathbf{r}_o; \kappa) \right] \cdot \hat{\mathbf{n}}_o d\sigma_o \\ & = \sum_j \int_{S_j} \left[G_0^+(\mathbf{r}'_j - \mathbf{r}_j; \kappa) \nabla \psi_j^+(\mathbf{r}_j; k) \right. \\ & \left. - \psi_j^+(\mathbf{r}_j; k) \nabla G_0^+(\mathbf{r}'_j - \mathbf{r}_j; \kappa) \right] \cdot \hat{\mathbf{n}}_j d\sigma_j \end{aligned} \quad (1)$$

where $\int_{S_o} \hat{\mathbf{n}}_o d\sigma_o$ and $\int_{S_j} \hat{\mathbf{n}}_j d\sigma_j$ are integrals over the surface of the cluster and of cell j respectively. A schematic view of the space partitioning of the solution $\psi^+(\mathbf{r}; k)$ is shown in figure 1. In our notations, $k = \sqrt{E}$ is the momentum of photoelectron, E is the energy of photoelectron measured from the vacuum level, and $\kappa \equiv \sqrt{k^2 - V_0}$ where V_0 is a constant potential in the interstitial region. In this paper, we adopt the condition $\kappa = k = \sqrt{E - V_0}$ without the outer sphere. For $\kappa = k$, the wavefunction $\psi^+(\mathbf{r}; k)$ satisfies the Lippmann-Schwinger equation

$$\psi^+(\mathbf{r}; k) = \phi_0(\mathbf{r}; k) + \int d\mathbf{r}' G_0^+(\mathbf{r} - \mathbf{r}'; k) V(\mathbf{r}') \psi^+(\mathbf{r}'; k) \quad (2)$$

with $\phi_0(\mathbf{r}; k)$ the free solution and $V(\mathbf{r})$ the potential. We assume that the wavefunctions $\psi_o^+(\mathbf{r}_o; k)$ and $\psi_j^+(\mathbf{r}_j; k)$

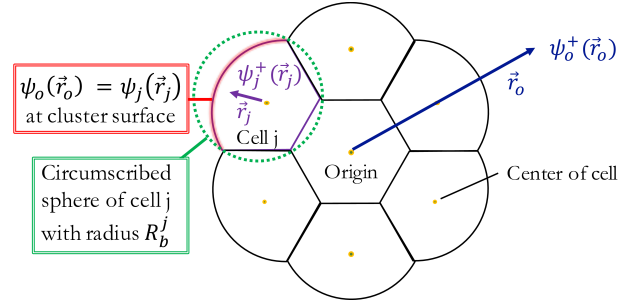


Figure 1. The wavefunction $\psi_j^+(\mathbf{r}_j)$ defined in cell j inside the cluster, the wavefunction $\psi_o^+(\mathbf{r}_o)$ for the outer region of the cluster, where we omit k .

respectively outside and inside of the cluster, can be expanded into local solutions $\Phi_L(\mathbf{r}_o; k)$ and $\Phi_L(\mathbf{r}_j; k)$ as

$$\psi_j^+(\mathbf{r}_j; k) = \sum_L A_L^j(\mathbf{k}) \Phi_L(\mathbf{r}_j; k) \quad (3)$$

$$\psi_o^+(\mathbf{r}_o; k) = \sum_L \tilde{A}_L^o(\mathbf{k}) J_L(\mathbf{r}_o; k) + \sum_L A_L^o(\mathbf{k}) \Phi_L(\mathbf{r}_o; k) \quad (4)$$

where $\tilde{A}_L^o(\mathbf{k}) \equiv i^l \mathcal{Y}_L(\hat{\mathbf{k}}) \sqrt{k/\pi}$. We employ the notation $L = (l, m)$ for the set of the angular azimuthal quantum number l and magnetic quantum number m . The \mathcal{Y}_L are the real spherical harmonics defined as a linear combination of the standard complex spherical harmonics Y_L [30, 31] as

$$\mathcal{Y}_L(\hat{\mathbf{k}}) = \sum_{m'} C_{mm'}^l Y_{lm'}(\hat{\mathbf{k}}) \quad (5)$$

where $C_{mm'}$ for $m > 0$ are

$$\begin{aligned} C_{mm}^l &= (-1)^m / \sqrt{2}, & C_{-m-m}^l &= 1 / \sqrt{2} \\ C_{-mm}^l &= -i(-1)^m / \sqrt{2}, & C_{-m-m}^l &= i / \sqrt{2}, \end{aligned}$$

and $C_{00}^l = 1$, otherwise $C_{mm'}^l = 0$. The functions $J_L(\mathbf{r}; k)$ and $\tilde{H}_L^+(\mathbf{r}; k)$ are defined as $J_L(\mathbf{r}; k) \equiv j_l(kr) \mathcal{Y}_L(\hat{\mathbf{r}})$ and $\tilde{H}_L^+(\mathbf{r}; k) \equiv -ik h_l(kr) \mathcal{Y}_L(\hat{\mathbf{r}})$ where j_l and h_l are respectively the spherical Bessel function and the spherical Hankel function of the first kind of order l . The expansion of the local solution into real spherical harmonics is

$$\Phi_L(\mathbf{r}_j; k) = \sum_{L'} R_{L'L}^j(r_j; k) \mathcal{Y}_{L'}(\hat{\mathbf{r}}_j). \quad (6)$$

In order to obtain the radial solution $R_{L'L}^j$, we employ the 3D Numerov method [22] to solve the three dimensional local Schrödinger equation. This avoids expanding the truncated potential into spherical harmonics, which is known to lead to Gibbs-type [32] convergence problems.

The matrix elements of the free electron Green's function in equation 1 expanded into real spherical harmonics on each site are called the real-space KKR structure factors and are given by [33]

$$G_{LL'}^{ij} \equiv 4\pi \sum_{L''} i^{l-l'+l''} C(L, L', L'') \tilde{H}_{L''}^+(\mathbf{R}_{ij}; k), \quad (7)$$

where $C(L, L', L'') \equiv \int d\hat{\mathbf{r}} \mathcal{Y}_L(\hat{\mathbf{r}}) \mathcal{Y}_{L'}(\hat{\mathbf{r}}) \mathcal{Y}_{L''}(\hat{\mathbf{r}})$ is a Gaunt coefficient of the real spherical harmonics.

On the basis of Green's theorem, the sum of the surface integrals on the truncated cells of the cluster in equation 1 is equal to the surface integral on its bounding sphere (the equality is valid also if $V_0 \neq 0$ as shown in Ref. [22]).

Equation 1 can then be reformulated in terms of the matrices S and E (which asymptotically behave as the sine and exponential function respectively) [34]

$$S_{L'L}^i \equiv (R_b^i)^2 \mathcal{W} \left[j_{l'}(kr_i), R_{L'L}^i(r_i; k) \right]_{r_i=R_b^i}, \quad (8)$$

$$E_{L'L}^i \equiv (R_b^i)^2 \mathcal{W} \left[-ikh_{l'}(kr_i), R_{L'L}^i(r_i; k) \right]_{r_i=R_b^i}. \quad (9)$$

Here, \mathcal{W} is the Wronskian at the surface of the bounding sphere of scattering site i , and R_b^i is the corresponding radius (See figure 1).

At this stage, we introduce the transition operator (or scattering T matrix) defined by

$$T^i \equiv -S^i (E^i)^{-1} \quad (10)$$

and the coefficients B_L^i related to the coefficients A_L^i by

$$B_L^i(\mathbf{k}) \equiv \sum_{L'} S_{L'L}^i A_{L'}^i(\mathbf{k}). \quad (11)$$

Inserting equations 3 and 7 in equality equation 1 and using equations 10 and 11, we obtain the following expression for the wavefunction,

$$\psi_i^+(\mathbf{r}; k) = \sum_L B_L^i(\mathbf{k}) \bar{\Phi}_L(\mathbf{r}) \quad (12)$$

where

$$B_L^i(\mathbf{k}) = \sum_{jL'} \tau_{jL'}^{ij} I_{L'}^j(\mathbf{k}), \quad (13)$$

$$\bar{\Phi}_L(\mathbf{r}) = \sum_{L'} ({}^tS)_{LL'}^{-1} \Phi_{L'}(\mathbf{r}), \quad (14)$$

$$\tau \equiv (T^{-1} - G)^{-1}, \quad (15)$$

$$I_L^j(\mathbf{k}) \equiv i^l \sqrt{\frac{k}{\pi}} e^{i\mathbf{k} \cdot \mathbf{R}_{io}} \mathcal{Y}_L(\hat{\mathbf{k}}). \quad (16)$$

Here, tS denotes the transpose of the matrix S . The amplitudes $B_L^i(\mathbf{k})$ are determined by the constraint that the wavefunction and its first derivative match smoothly to the outer multiple scattering scheme at the surface at each cell. The multiple scattering matrix τ (or scattering path operator) is constructed from the transition operator and free electron Green's function defined in equation 7.

2.2. Expression of Photoelectron Diffraction Cross-section

In this subsection, we study the photoelectron diffraction cross-section based on Fermi's golden rule within the single channel approximation. We assume that the wavefunctions of the core electron, photoelectron, and valence electrons do not mix-up and can be treated independently. Under the conditions mentioned above and within the electric dipole approximation, the many body electric dipole matrix element reduces to a single particle one. Then the general expression of the photoelectron

diffraction cross-section along direction $\hat{\mathbf{k}}$ from an emitter atom on site i , is given by

$$I(\mathbf{k}, \hat{\boldsymbol{\varepsilon}}) = 8\pi^2 \alpha \hbar \omega \sum_{m_c} \left| \langle \psi_i^-(\mathbf{r}; \mathbf{k}) | \hat{\boldsymbol{\varepsilon}} \cdot \mathbf{r}_i | \phi_{L_c}^c(\mathbf{r}_i) \rangle \right|^2, \quad (17)$$

where $\phi_{L_c}^c(\mathbf{r})$ with the short-hand notation $L_c = (l_c, m_c)$ is the initial core state, α is the fine structure constant, $\hbar\omega$ is the photon energy, $\hat{\boldsymbol{\varepsilon}}$ is the polarisation vector of photon. We neglect the spin polarisation in the photoemission process, therefore introducing a factor two into the formula above.

Using the multiple scattering expression for the photoelectron wavefunction $\psi_i^+(\mathbf{r}; \mathbf{k})$ in equation 12, we obtain the following formula for the MFPADs

$$I(\mathbf{k}, \hat{\boldsymbol{\varepsilon}}) = 8\pi^2 \alpha \hbar \omega \sum_{m_c} \left| \sum_L B_L^{i*}(\mathbf{k}) M_{L_c L}(\hat{\boldsymbol{\varepsilon}}) \right|^2, \quad (18)$$

where

$$M_{L_c L}(\hat{\boldsymbol{\varepsilon}}) \equiv \int d\mathbf{r} \bar{\Phi}_L(\mathbf{r}) \hat{\boldsymbol{\varepsilon}} \cdot \mathbf{r} \phi_{L_c}^c(\mathbf{r}),$$

is the transition matrix which describes the excitation by X-rays of polarization $\hat{\boldsymbol{\varepsilon}}$ of an electron from a core orbital $\phi_{L_c}^c$.

2.3. Polarization Average of Photoelectron Cross-section

The polarization average of the MFPADs is obtained by angular integration of the polarization

$$\begin{aligned} \langle I(\mathbf{k}) \rangle_{\boldsymbol{\varepsilon}} &\equiv \frac{1}{4\pi} \int d\hat{\boldsymbol{\varepsilon}} I(\mathbf{k}, \hat{\boldsymbol{\varepsilon}}) \\ &= 2\pi \alpha \hbar \omega \sum_{m_c L L'} B_L^{i*}(\mathbf{k}) B_{L'}^i(\mathbf{k}) \int d\hat{\boldsymbol{\varepsilon}} M_{L_c L}(\hat{\boldsymbol{\varepsilon}}) M_{L_c L'}^*(\hat{\boldsymbol{\varepsilon}}). \end{aligned}$$

Since the electric dipole operator can be expanded as $\hat{\boldsymbol{\varepsilon}} \cdot \mathbf{r} = (4\pi/3) r \sum_m \mathcal{Y}_{1m}(\hat{\boldsymbol{\varepsilon}}) \mathcal{Y}_{1m}(\hat{\mathbf{r}})$ [35], the integration reduces to a sum of Cartesian components,

$$\begin{aligned} &\int d\hat{\boldsymbol{\varepsilon}} M_{L_c L}(\hat{\boldsymbol{\varepsilon}}) M_{L_c L'}^*(\hat{\boldsymbol{\varepsilon}}) \\ &= \frac{4\pi}{3} \left[M_{L_c L}(\hat{\mathbf{x}}) M_{L_c L'}^*(\hat{\mathbf{x}}) + M_{L_c L}(\hat{\mathbf{y}}) M_{L_c L'}^*(\hat{\mathbf{y}}) + M_{L_c L}(\hat{\mathbf{z}}) M_{L_c L'}^*(\hat{\mathbf{z}}) \right]. \end{aligned}$$

Thus, we obtain the following expression for the PA-MFPADs

$$\langle I(\mathbf{k}) \rangle_{\boldsymbol{\varepsilon}} = \frac{1}{3} [I(\mathbf{k}, \hat{\mathbf{x}}) + I(\mathbf{k}, \hat{\mathbf{y}}) + I(\mathbf{k}, \hat{\mathbf{z}})].$$

We see that averaged intensity of the MFPADs over the polarization vector along x , y and z -axes reduces to the intensity of the PA-MFPADs.

The intensity of the the PA-MFPADs denoted as $\langle I(\mathbf{k}) \rangle_{\boldsymbol{\varepsilon}}$ is given as

$$\begin{aligned} \langle I(\mathbf{k}) \rangle_{\boldsymbol{\varepsilon}} &= \frac{8\pi^2 \alpha \hbar \omega}{3} \sum_{n, m_c} \left| \sqrt{\frac{4\pi}{3}} \sum_{LL'} B_L^{i*}(\mathbf{k}) \right. \\ &\quad \left. \times C(L_c, 1n, L') \int dr r^3 R_{L'L}(r; k) R_{L_c}^c(r) \right|^2. \end{aligned} \quad (19)$$

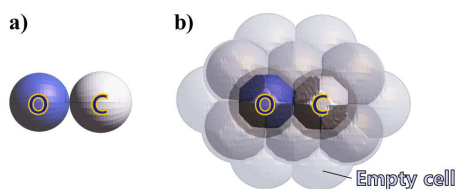


Figure 2. Cell images of CO used for our multiple scattering calculations, (a) for the Muffin-tin approximation with two spherical non overlapping atomic spheres and (b) for the Full-potential method with two Voronoi atomic cells, and 22 truncated spherical cells (the so-called empty cells) which contain only electron charge density (no nucleus inside). The positions of cells are arranged in a BCC structure.

3. Computational Details

3.1. Quantum Chemistry Calculation of the Electronic Structure

In the following, we specialize to a two-color XFEL pump-probe experiment. The pump pulse removes an electron from the 2σ (C(1s)) orbital of CO which results in the subsequent Auger ionization to, e.g., the singlet $5\sigma^{-2}$ states [36, 37, 38]. The probe pulse further eliminates an electron from the $1\sigma^{-1}$ (O(1s)) orbital. This pump-probe process finally produces a doublet $1\sigma^{-1}5\sigma^{-2}$ state. All electronic structure calculations in CO were carried out with the MOLCAS 8.2 quantum chemical package [39]. The electrostatic potential of the doublet $1\sigma^{-1}\sigma^{-2}$ state of CO^{3+*} as a function of C-O bond length for the multiple scattering calculation were constructed at the multireference second-order perturbation theory with restricted active space (RASPT2) level of theory [40, 41]. A ionization potential electron affinity (IPEA) shift of 0.25 a.u. was introduced to reduce the intruder problem [42]. The reference wavefunctions for the RASPT2 calculations were computed at the state-averaged Restricted Active Space self-consistent field (SA-RASSCF) level of theory [43]. The 10-low-lying doublet states were considered without symmetry, and their average energy was minimized with the equal weight. For all RASPT2 and SA-RASSCF calculations, we included 10 spatial orbitals constructed mainly from $1s$, $2s$, $2p$ orbitals of carbon and oxygen atoms, that is 1σ , 2σ , 3σ , 4σ , $2 \times 1\pi$, 5σ (HOMO), $2 \times 2\pi$ (LUMO) and 6σ as active space, where the maximum occupation of the 1σ orbital is restricted to one to describe the core-hole in this orbital. The 11 electrons in the active orbitals were treated as active electrons. The ANO-RCC-VQZP basis set [44] was consistently used. Relativistic effects were taken into account through the second order Douglas-Kroll-Hess [45] and mean-field spin-orbit [46] Hamiltonians.

This RASPT2 treatment is essential for an accurate evaluation of the chemical shift in photoelectron energy and photoelectron momentum. The second order perturbation and relativistic corrections affect only the energetics in this

system. The core orbital is identical to the O(1s) Hartree-Fock (HF) orbital of CO²⁺. We used the natural orbitals obtained from RASPT2 calculations for the input of the electron density calculations, however the RASPT2 natural orbitals are almost identical to those from RASSCF. Thus, the RASPT2 density is almost identical to the RASSCF one, and the electron density triple cation is close to that of a HF calculation on the ion especially for the $1\sigma^{-1}5\sigma^{-2}$ state in the Franck-Condon region. We also calculated the $1\sigma^{-1}4\sigma^{-1}5\sigma^{-1}$ and $1\sigma^{-1}5\sigma^{-1}1\pi^{-1}$ states for comparison. However, they have multiconfiguration characters and RASSCF (or RASPT2) density is essentially different from HF ones. In addition, the contribution of the $1\sigma^{-1}5\sigma^{-2}$ configuration on the RASSCF wavefunction varies when we elongate the C-O bond length. This is another reason that the RASSCF (or RASPT2) treatment is essential.

3.2. Multiple Scattering Calculation for Full-potential and Muffin-tin cases

The scattering matrix τ and the transition matrices T were calculated with the FPMS code [21, 22] within the framework of the multiple scattering approach. The photoelectron diffraction calculations were performed with the MsSpec code [47], using these matrices as an input. For Full-potential calculations, we need to add empty cells (pseudo atomic cells with electron charge density but no nucleus) in order to account for the charge density outside the (Voronoi) atomic cells. We have used 22 empty cells to embed the carbon and oxygen cells within a BCC structure as shown in figure 2. The multiple scattering calculation was found to converge at $l_{max} = 6$ and 8 for the Muffin-tin approximation and the Full-potential method, respectively. The same l_{max} was used for the expansion of the wavefunction $\psi_j^+(\mathbf{r}; k)$ into local solutions and the expansion of each local solution into spherical harmonics. Following Kazama *et al.* [48], the kinetic energy of the photoelectron was estimated as $k = \sqrt{E - V_0}$, where V_0 is the surface average of the potential of the cluster. This V_0 is the threshold for the continuum and bound state. The wavefunction outside the cells is a plane wave of momentum k .

In order to estimate the T -matrices for each cell, we solved the local Schrödinger equations with an optical potential which is the sum of the static Coulomb potential, namely the Hartree potential, and the exchange-correlation potential. To take into account the electron correlation between the ejected core electron and the $N - 1$ remaining electrons, we used a Hedin-Lundqvist potential [49, 50] which is a self-energy used in the field of solid state physics. This potential is based on the GW approximation with a non-SCF Green's function G , a screened potential W and a single plasmon pole approximation, and allows to model satisfactorily the scattering optical potential in the multiple scattering calculations. It is known however

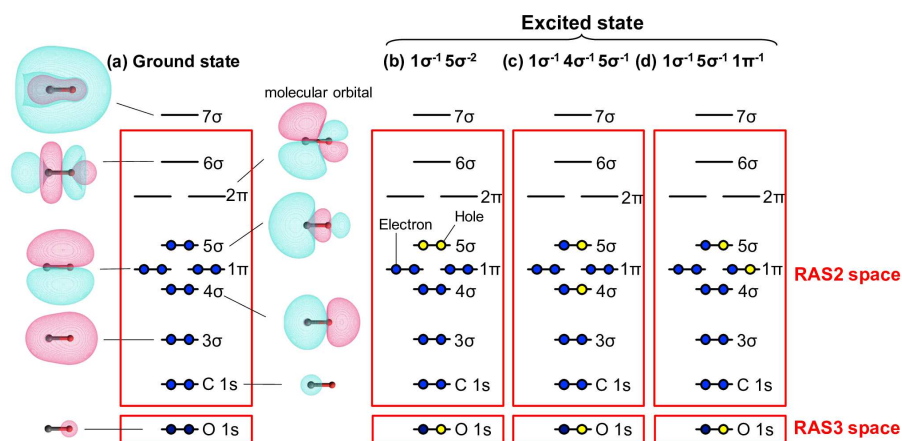


Figure 3. Major electronic configurations of (a) the ground state and the most probable excited states after oxygen 1s excitation (b) $1\sigma^{-1}5\sigma^{-2}$, (c) $1\sigma^{-1}4\sigma^{-1}5\sigma^{-1}$ and (d) $1\sigma^{-1}5\sigma^{-1}1\pi^{-1}$, respectively. The excited states (b), (c) and (d) are the dicationic states populated via the C (1s) KVV Auger decay with a core hole created by the second pulse in the oxygen 1s orbital, that is to say CO³⁺. Blue and yellow dots in the energy levels represent respectively electrons and holes. The shapes of the molecular orbitals are illustrated. Active spaces (RAS2 and RAS3 space) for RASSCF calculations are assigned in the red boxes.

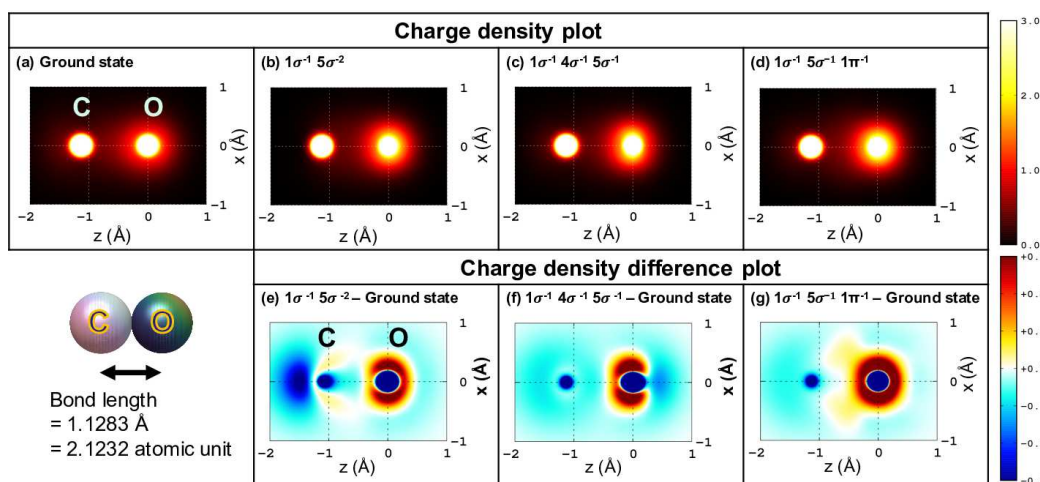


Figure 4. Electron charge density plots of CO in the molecular axis plane for (a) the ground state and the excited states (b) $1\sigma^{-1}5\sigma^{-2}$, (c) $1\sigma^{-1}4\sigma^{-1}5\sigma^{-1}$ and (d) $1\sigma^{-1}5\sigma^{-1}1\pi^{-1}$ defined in figure 3. These are the dicationic states populated via the C (1s) KVV Auger decay with a core hole created by the second pulse in the oxygen 1s orbital, that is to say CO³⁺. The electronic structures are calculated with the ANO-RCC-VQZP basis set, where the oxygen atom is set at the origin and the C-O bond length is fixed to 1.1283 Å for all the calculations. The oxygen 1s hole in the RAS3 space is kept during the calculations for the excited states. The plots (e)-(g) are electron charge density difference plots between (a) the ground state and the corresponding excited state among (b)-(d), respectively.

that its imaginary part produces a rather strong damping effect [22, 21], especially for light elements such as carbon and oxygen, hence we used only the real part in our calculations. Since CO molecules do not have any particular direction perpendicular to the molecular axis, the intensity of photoelectron was averaged over the azimuth angle around that axis.

The electron charge density for the multiple scattering calculations has been prepared following two different prescriptions. In the first one, which we refer to as "non-SCF" (non-self-consistent), the molecular potential and the electron charge density were constructed by a simple superposition of the free atomic densities. The

free atom calculations were performed with the Desclaux code [51] which employs a multi-configuration relativistic Dirac-Fock theory, and the excited states were calculated with a fully relaxed core hole. The second one, which we call "SCF", employs the electron charge density calculated from MOLCAS 8.2 with the help of a Hermite Gaussian basis functions set [52] and the (Coulomb) static part of the scattering potential calculated under the McMurchie-Davidson scheme [52] with a Boys function [53]. The details can be found in Ref. [54].

In the muffin-tin calculations, for both prescriptions, the electron charge density and the static part of the potential were spherically averaged. For the muffin-tin

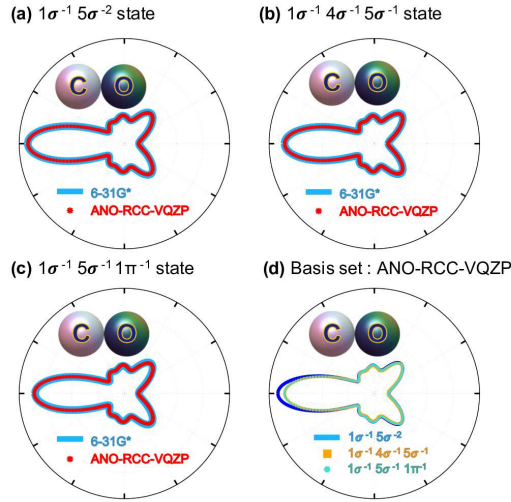


Figure 5. Influence of the basis functions on the PA-MFPADs at 100 eV kinetic energy of the photoelectron with 1.1283 Å of C-O bond length (equilibrium bond length in ground state). The calculations are performed within the Full-potential method using 6-31G* and the ANO-RCC-VQZP basis sets. (a) $1\sigma^{-1}5\sigma^{-2}$, (b) $1\sigma^{-1}4\sigma^{-1}5\sigma^{-1}$ and (c) $1\sigma^{-1}5\sigma^{-1}1\pi^{-1}$ state respectively. These are the dicationic states populated via the C (1s) KVV Auger decay with a core hole created by the second pulse in the oxygen 1s orbital, that is to say CO³⁺. (d) Influence of the electronic structure type on the PA-MFPADs. We compare the PA-MFPADs for the following electronic structures: $1\sigma^{-1}5\sigma^{-2}$, $1\sigma^{-1}4\sigma^{-1}5\sigma^{-1}$ and $1\sigma^{-1}5\sigma^{-1}1\pi^{-1}$ state where the basis set is ANO-RCC-VQZP.

spheres, we used touching but non overlapping C and O atomic spheres. The sphere radii were estimated for each bond length by the Norman criterion [55] and are roughly proportional to the ionic radius of the atom in the periodic table. An empirical prescription to improve the results is to use overlapping spheres, 10~15%, to account approximately for the presence of covalent electrons (see Refs. [56, 55]). This approximation is called the Atomic-Sphere Approximation (ASA) in LMTO and KKR [57]. However, as it is not our scope in this work to empirically optimise the results through tentative overlapping, we have kept to the touching spheres. For V_0 , we have used the value obtained from our Full-potential calculations.

4. Results

4.1. Dependence on Electronic Structures

We consider three states, $1\sigma^{-1}5\sigma^{-2}$, $1\sigma^{-1}4\sigma^{-1}5\sigma^{-1}$ and $1\sigma^{-1}5\sigma^{-1}1\pi^{-1}$, as shown in figure 3. These states are the dicationic states populated via the C (1s) KVV Auger decay [38] with a core hole created by the second pulse in the oxygen 1s orbital.

In figure 4 the ground state and excited states electron charge densities are displayed in the upper row and the electron charge density difference plots, between each excited state and the ground state, are shown in lower row.

As $1\sigma^{-1}4\sigma^{-1}5\sigma^{-1}$ in (c) has a C_{2v} symmetry around the molecular axis, we chose the xz -plane to lay the orbital in order to see its anisotropy. All the other electronic configurations have a $C_{\infty v}$ symmetry around the axis. These comparisons show the change of charge distributions varying with electronic configuration.

Next, we studied the influence of the electronic structure on the PA-MFPADs. Figure 5 shows the results of PA-MFPADs simulations performed for the three electron configurations using the 6-31G* (small, double-zeta + valence polarization) and the ANO-RCC-VQZP (large, quadratic-zeta + valence polarization) basis sets. The results clearly indicate that the PA-MFPADs are not very sensitive to the electronic structure in this high energy regime. Therefore, in the following subsections, we will use the $1\sigma^{-1}5\sigma^{-2}$ configuration as a representative electronic configuration using the ANO-RCC-VQZP.

4.2. Dependence on Bond Length

The PA-MFPADs calculated as a function of the C-O bond length are shown in figure 6. The forward-intensity $\langle I(k, \theta = 0^\circ) \rangle_\varepsilon$ corresponds to the largest lobe, which is directed along the bond towards the carbon atom. This lobe is due to the so-called focusing effect of photoelectrons by the carbon atom. The backward-intensity $\langle I(k, \theta = 180^\circ) \rangle_\varepsilon$ is in the opposite direction, and it oscillates between the peak top and the valley of the lobe as a function of R . Within the framework of the Plane Wave single-scattering approximation of the electron Green's function in equation 7 (see for instance the EXAFS formula [58]), one period of the oscillation corresponds to an increase by $\Delta R = \pi/k$ in R . There are several small lobes between the forward and backward directions, which move from backward to forward as R increases. The number of lobes is incremented every one period of oscillation of the backward-intensity peak. Labelling angles θ_1 and θ_2 for two neighbouring lobes ($\theta_1 < \theta_2$), we have approximately $R = 2\pi/k(\cos\theta_1 - \cos\theta_2)$. Thus, the PA-MFPADs do contain the information about the bond length. We will discuss this relation in more detail in the companion paper [59].

4.3. Dependence on Shape of Potential

In order to evaluate the effect of the Muffin-tin approximation on the PA-MFPADs, we compare in figure 7 the oxygen 1s PA-MFPADs of CO²⁺ calculated with the Muffin-tin approximation to the corresponding one obtained from the Full-potential method. The major C (1s) KVV Auger decay channels in the low-energy region were estimated according to the ADC(2) calculations by Cederbaum *et al.* [38]. The kinetic energy of the photoelectron is chosen to be 100 eV on the basis of the widely supported idea that photoelectron spectroscopy is less sensitive to the details of the electronic structure and the electron charge density in a sufficiently high

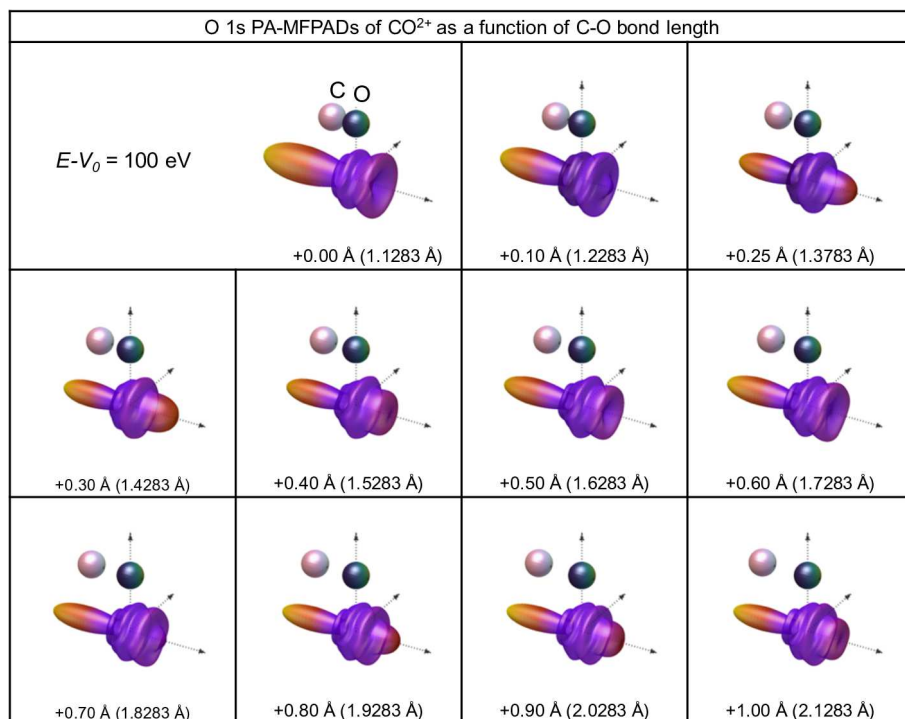


Figure 6. The oxygen 1s PA-MFPADs of CO²⁺ as a function of the C-O bond length R from 1.1283 Å (equilibrium bond length in ground state) to 2.1283 Å. All the calculations were performed within the Full-potential method for the excited state $1\sigma^{-1}5\sigma^{-2}$ (i.e. O $1s^{-1}$ HOMO⁻² which is triply charged CO, namely CO³⁺) with a photoelectron kinetic energy of 100 eV.

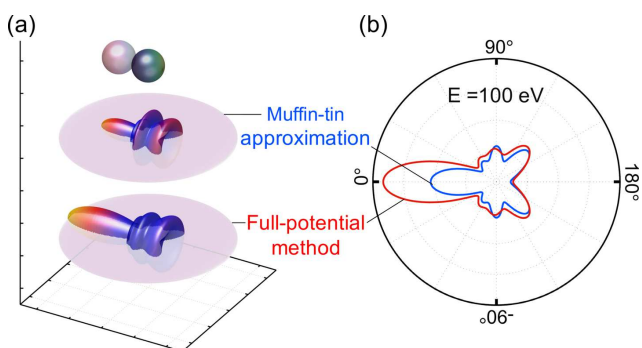


Figure 7. The oxygen 1s PA-MFPADs of CO²⁺ in the excited state $1\sigma^{-1}5\sigma^{-2}$ (i.e. O $1s^{-1}$ HOMO⁻² which is triply charged CO, namely CO³⁺) with 100 eV of photoelectron kinetic energy. The oxygen atom is located at the origin and the azimuthal angle is defined from the direction of the carbon atom. (a) The oxygen 1s PA-MFPADs within the Muffin-tin approximation is shown in the upper plane and that within the Full-potential method is displayed in lower plane. (b) Comparison of the PA-MFPADs between Muffin-tin approximation (blue line) and Full-potential method (red line).

energy regime (≥ 100 eV) [22].§ We see that the PA-MFPADs patterns are clearly distinct from each other. The largest contribution to the forward-intensity comes

§ The calculated vertical O($1s^{-1}$) ionization energy from the lowest singlet state of CO²⁺ were found to be 564-569 eV at the RASPT2/ANO-RCC-VQZP level of theory depending the C-O bond length R (chemical shifts). This means that we have only 5 % and 2-3 % errors on the photoelectron energy and momentum, respectively.

from the forward-scattering by the carbon atom which induces a focusing effect. This forward-scattering is due here to a weak potential. Since such a weak potential is essentially left outside of the Muffin-tin spheres in the case of short distances, the forward-intensity is certainly underestimated in the Muffin-tin approximation. In figure 8, we show a series of comparisons between the Muffin-tin approximation and the Full-potential method for multiple scattering calculations of the oxygen 1s PA-MFPADs of CO²⁺ as a function of the C-O bond length R from 1.1283 Å (equilibrium bond length in ground state) to 2.1283 Å. All the calculations were performed for the excited state $1\sigma^{-1}5\sigma^{-2}$ (i.e. O $1s^{-1}$ HOMO⁻²) with a photoelectron kinetic energy of 100 eV. As noted in figure 7, the forward-intensity peak is significantly underestimated by the Muffin-tin approximation at near equilibrium distance. Besides, the peak positions between the forward- and backward-intensity peaks start to differ with the increase in R between the results in the Muffin-tin approximation and the Full-potential method.

As we notice in figure 9, the frequency of the oscillations of the backward-intensity is almost $2kR$ for both cases. Indeed, this corresponds exactly to the EXAFS oscillation frequency. In this high energy regime, i.e. in the EXAFS regime, single scattering towards the backward direction is the main contribution of the backward-intensity, so that we expect that we may observe this EXAFS-like oscillation in the backward-intensity as in EXAFS. In the

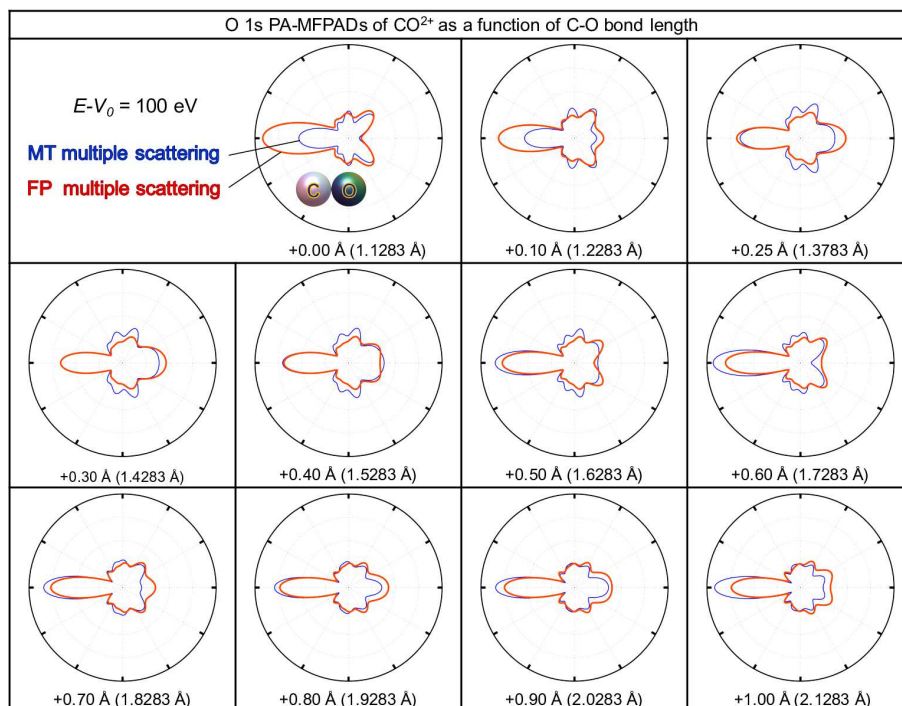


Figure 8. The oxygen 1s PA-MFPADs of CO²⁺ as a function of the C-O bond length R from 1.1283 Å (equilibrium bond length in ground state) to 2.1283 Å for a photoelectron kinetic energy of 100 eV. All the calculations were performed with the excited state $1\sigma^{-1}5\sigma^{-2}$ (i.e. O $1s^{-1}$ HOMO⁻² which is triply charged CO, namely CO³⁺). Blue and red lines indicate the results of multiple scattering calculation using the Muffin-tin approximation and the Full-potential method, respectively.

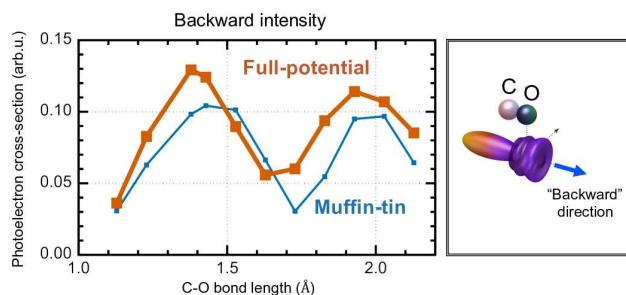


Figure 9. Backward-intensities of the oxygen 1s PA-MFPADs of CO²⁺ as a function of the C-O bond length R from 1.1283 Å (equilibrium bond length in ground state) to 2.1283 Å for $1\sigma^{-1}5\sigma^{-2}$ state (i.e. O $1s^{-1}$ HOMO⁻² which is triply charged CO, namely CO³⁺). Dark blue and orange lines indicate multiple scattering calculation results within the Muffin-tin approximation and the Full-potential method, respectively.

case of the oxygen 1s PA-MFPADs of CO²⁺, the back-scattering is caused mainly by the strong (core) potential very near the center of the carbon atom. At first sight, it may seem strange to have so much difference between the two calculations, since the electron charge densities are almost spherically symmetric in the Full-potential case. In fact, it is the contribution of the forward-scattering by the oxygen atom which accounts for the difference. This forward-scattering occurs at the second scattering order, along the pathway going from the carbon atom to the

detector. Its influence, especially through the phase of the forward scattering amplitude, $\psi(k, \theta = 0^\circ)$, appears in the EXAFS oscillation as $\cos(2kR + \psi(k, \theta = 0^\circ) + \psi(k, \theta = 180^\circ))$. Since forward-scattering is important even for a weak potential, it is more sensitive to fine details of the electron charge density and therefore, it depends strongly on the modelling of the scattering potential. Thus the error in the Muffin-tin approximation appears to make the difference of peak/valley positions for the two calculations in figure 9.

4.4. Toward Reaction Dynamics Imaging using PA-MFPADs based on Ab-initio Full-potential Multiple Scattering Theory

Finally, we would like to consider the potential targets of the reaction dynamics imaging simulations using PA-MFPADs based on the Full-potential multiple scattering theory, just beyond the dissociation of the dication of diatomic molecules.

A possible extension that may be monitored by the present technique is the fragmentation of the methanol dication. There are at least two major fragmentation channels. One is the direct C-O bond breaking [60]. This process is very similar to the dissociation of the diatomic molecule, which we have considered in the present work. The other is the molecular dissociation into CO⁺ and H₃⁺. In this process, roaming of H₂ takes place and extraction of

H⁺ from CH or OH sites follows [61]. The timescale of this process is ~ 100 fs. We should be able to distinguish between these two pathways, both experimentally and theoretically, by the momenta of fragment ions that define the molecular axis or reaction plane to be observed for O 1s PA-MFPADs via the C(1s) pump O(1s) probe scheme.

A case a little more complex but still feasible with the present method could be the X-ray induced fragmentation of doubly charged amino acids such as glycine [62], serine [63], etc. A typical first step of the decomposition is the COOH⁺ ejection [63, 64, 65] with a time scale of 10-100 fs [62, 63, 64, 65]. Capturing the COOH⁺ loss dynamics could be achieved by the C(1s) pump N(1s) probe scheme.

Furthermore, many photochemical reactions of polyatomic molecules with hetero-atoms for the photoelectron source could also become attractive targets. For example, ultraviolet induced femtosecond H loss of pyrrole via ¹ $\pi\pi^*$ and ¹ $\pi\sigma^*$ states [66] will be a suitable target since its N atom is applicable for the photoelectron source and the dissociating H atom locates just next to the N atom. These molecules will also become good potential targets of the imaging experiments with the PA-MFPADs with the two-color XFEL light source.

From the theoretical points of view, the on-the-fly reaction dynamics calculations [67, 68, 69, 70, 60, 71, 72, 73, 74, 75] and ab-initio core-hole spectroscopy [71, 76, 77, 78, 79, 80, 81] for these polyatomic molecules are already feasible. It will also be helpful to improve the efficiency of the electrostatic potential evaluation and the Full-potential multiple scattering calculations by further tuning including massive parallelization to push its interplay with the experiment and reaction dynamics theory forward. In addition, analytical formulae that extract structural dynamics from the complex scattering results will also be useful [59].

5. Conclusions

We have studied theoretically the PA-MFPADs emitted from the 1s orbital of oxygen atom of dissociating dicationic carbon monoxide CO²⁺. Within the framework of multiple scattering theory, we have investigated the influence of the Muffin-tin approximation and the role of the potential in different excited states, with electron charge densities calculated using the RASPT2 method in order to model properly the influence of the core hole in the final state. The Full-potential theory takes into account the electron charge density outside the physical atomic cells by using simultaneously Voronoi polyhedra and truncated spheres.

Despite the fact that the Muffin-tin approximation was giving similar results as the Full-potential calculation above 100 eV for XANES [22], we observe here significant differences in the PA-MFPADs. This may be explained by the general optical theorem which states for *real potentials* that the integrated photoemission over the whole solid angle

equals the X-ray absorption [22, 82]. A consequence of this theorem is that in XANES, even if there is a difference in angular distribution between the Muffin-tin approximation and the Full-potential method, this difference will be smeared out by the angular integration. Moreover, even in the case of long bond lengths, where the atomic approximation works, we found a significant difference in the PA-MFPADs between the Muffin-tin approximation and the Full-potential method. The consequence is that we need to use the Full-potential multiple scattering theory to study structure dynamics using FELs and Synchrotron even in the high energy region.

We have also studied the PA-MFPADs from different excited states of the Auger final state. We have found that the type of excited states does not affect significantly the PA-MFPADs, though the difference in the electronic structure was not negligible. The relationship between the PA-MFPADs patterns and the C-O bond length will be discussed in detail within the multiple scattering theory in the companion article [59].

Acknowledgement

We would like to acknowledge C. R. Natoli for fruitful discussions. This work was accomplished under the program of the Dynamic Alliance for Open Innovation Bridging Human, Environment and Materials program and Cooperative Research Program of "Network Joint Research Center for Materials and Devices". K. H. acknowledges funding by JSPS KAKENHI under Grant No. 18K05027 and 17K04980. K. Y. is grateful for the financial support from Building of Consortia for the Development of Human Resources in Science and Technology, MEXT.

References

- [1] D. P. Woodruff. Photoelectron diffraction: from phenomenological demonstration to practical tool. *Applied Physics A*, 92:439–445, 2008.
- [2] E. Shigemasa, J. Adachi, M. Oura, and A. Yagishita. Angular Distributions of 1s σ Photoelectrons from Fixed-in-Space N₂ Molecules. *Physical Review Letters*, 74(3):359–362, January 1995.
- [3] O. Jagutzki, A. Cerezo, A. Czasch, R. Dörner, M. Hattas, Min Huang, V. Mergel, U. Spillmann, K. Ullmann-Pfleger, T. Weber, H. Schmidt-Böcking, and G. D. W. Smith. Multiple hit readout of a microchannel plate detector with a three-layer delay-line anode. *IEEE Transactions on Nuclear Science*, 49(5):2477–2483, 2002.
- [4] J. Ullrich, R. Moshhammer, A. Dorn, R. Dörner, L. Ph. H. Schmidt, and H. Schmidt-Böcking. Recoil-ion and electron momentum spectroscopy: reaction-microscopes. *Reports on Progress in Physics*, 66(9):1463–1545, aug 2003.
- [5] A. Landers, Th. Weber, I. Ali, A. Cassimi, M. Hattas, O. Jagutzki, A. Nauert, T. Osipov, A. Staudte, M. H. Prior, H. Schmidt-Böcking, C. L. Cocke, and R. Dörner. Photoelectron Diffraction Mapping: Molecules Illuminated from Within. *Physical Review Letters*, 87:013002, Jun 2001.
- [6] E D Poliakoff and R R Lucchese. Evolution of photoelectron–vibrational coupling with molecular complexity. *Physica Scripta*, 74(5):C71–C79, oct 2006.

- [7] E Plésiat, P Decleva, and F Martín. Vibrationally resolved photoelectron angular distributions from randomly oriented and fixed-in-space N₂ and CO molecules. *Journal of Physics B: Atomic, Molecular and Optical Physics*, 45(19):194008, sep 2012.
- [8] N A Cherepkov, G Raseev, J Adachi, Y Hikosaka, K Ito, S Motoki, M Sano, K Soejima, and A Yagishita. K-shell photoionization of CO: II. Determination of dipole matrix elements and phase differences. *Journal of Physics B: Atomic, Molecular and Optical Physics*, 33(20):4213–4236, September 2000.
- [9] L Kaiser, K Fehre, N M Novikovskiy, J Stindl, D Tsitsonis, G Gopakumar, I Unger, J Söderström, O Björneholm, M Schöffler, T Jahnke, R Dörner, F Trinter, and Ph V Demekhin. Angular emission distribution of O 1s photoelectrons of uniaxially oriented methanol. *Journal of Physics B: Atomic, Molecular and Optical Physics*, 53(19):194002, aug 2020.
- [10] N Saito, A De Fanis, K Kubozuka, M Machida, M Takahashi, H Yoshida, I H Suzuki, A Cassimi, A Czasch, L Schmidt, R D rner, K Wang, B Zimmermann, V McKoy, I Koyano, and K Ueda. Carbon K-shell photoelectron angular distribution from fixed-in-space CO₂ molecules. *Journal of Physics B: Atomic, Molecular and Optical Physics*, 36(1):L25–L30, dec 2002.
- [11] Daniel Rolles, Markus Braune, Slobodan Cvejanović, Oliver Geßner, Rainer Hentges, Sanja Korica, Burkhard Langer, Toralf Lischke, Georg Prümper, Axel Reinköster, Jens Viehhaus, Björn Zimmermann, Vincent McKoy, and Uwe Becker. Photoelectron diffraction: from phenomenological demonstration to practical tool. *Nature*, 437:711–715, 2005.
- [12] S. K. Semenov, N. A. Cherepkov, G. H. Fecher, and G. Schönhense. Generalization of the atomic random-phase-approximation method for diatomic molecules: N₂ photoionization cross-section calculations. *Physical Review A*, 61:032704, Feb 2000.
- [13] S. K. Semenov and N. A. Cherepkov. Generalization of atomic random-phase-approximation method for diatomic molecules. II. N₂ K-shell photoionization. *Physical Review A*, 66:022708, Aug 2002.
- [14] R. E. Stratmann and Robert R. Lucchese. A graphical unitary group approach to study multiplet specific multichannel electron correlation effects in the photoionization of O₂. *The Journal of Chemical Physics*, 102(21):8493–8505, 1995.
- [15] R. E. Stratmann, Robert W. Zurales, and Robert R. Lucchese. Multiplet-specific multichannel electron-correlation effects in the photoionization of NO. *The Journal of Chemical Physics*, 104(22):8989–9000, 1996.
- [16] M. Stener, G. Fronzoni, and P. Decleva. Time-dependent density-functional theory for molecular photoionization with noniterative algorithm and multicenter B-spline basis set: CS₂ and C₆H₆ case studies. *The Journal of Chemical Physics*, 122(23):234301, 2005.
- [17] Etienne Plésiat, Piero Decleva, and Fernando Martín. Relationship between polarization-averaged molecular-frame photoelectron angular distributions and geometry. *Physical Review A*, 88:063409, Dec 2013.
- [18] Hironobu Fukuzawa, Syuhei Yamada, Yuta Sakakibara, Tetsuya Tachibana, Yuta Ito, Tsukasa Takanashi, Toshiyuki Nishiyama, Tsukasa Sakai, Kiyonobu Nagaya, Norio Saito, Masaki Oura, Mauro Stener, Piero Decleva, and Kiyoshi Ueda. Probing gaseous molecular structure by molecular-frame photoelectron angular distributions. *The Journal of Chemical Physics*, 151(10):104302, 2019.
- [19] C.S. Fadley, S. Thevuthasan, A.P. Kaduwela, C. Westphal, Y.J. Kim, R. Ynzunza, P. Len, E. Tober, F. Zhang, Z. Wang, S. Ruebush, A. Budge, and M.A. Van Hove. Photoelectron diffraction and holography: Present status and future prospects. *Journal of Electron Spectroscopy and Related Phenomena*, 68:19 – 47, 1994.
- [20] Misato Kazama, Takashi Fujikawa, Naoki Kishimoto, Tomoya Mizuno, Jun-ichi Adachi, and Akira Yagishita. Photoelectron diffraction from single oriented molecules: Towards ultrafast structure determination of molecules using x-ray free-electron lasers. *Physical Review A*, 87:063417, Jun 2013.
- [21] Keisuke Hatada, Kuniko Hayakawa, Maurizio Benfatto, and Calogero R. Natoli. Full-potential multiple scattering for x-ray spectroscopies. *Physical Review B*, 76:060102, Aug 2007.
- [22] Keisuke Hatada, Kuniko Hayakawa, Maurizio Benfatto, and Calogero R Natoli. Full-potential multiple scattering theory with space-filling cells for bound and continuum states. *Journal of Physics: Condensed Matter*, 22(18):185501, apr 2010.
- [23] Junqing Xu, Peter Krüger, Calogero R. Natoli, Kuniko Hayakawa, Ziyu Wu, and Keisuke Hatada. X-ray absorption spectra of graphene and graphene oxide by full-potential multiple scattering calculations with self-consistent charge density. *Physical Review B*, 92:125408, Sep 2015.
- [24] J. B. Williams, C. S. Trevisan, M. S. Schöffler, T. Jahnke, I. Bocharova, H. Kim, B. Ulrich, R. Wallauer, F. Sturm, T. N. Rescigno, A. Belkacem, R. Dörner, Th. Weber, C. W. McCurdy, and A. L. Landers. Imaging Polyatomic Molecules in Three Dimensions Using Molecular Frame Photoelectron Angular Distributions. *Physical Review Letters*, 108:233002, Jun 2012.
- [25] Hironobu Fukuzawa, Robert R. Lucchese, Xiao-Jing Liu, Kentaro Sakai, Hiroshi Iwayama, Kiyonobu Nagaya, Katharina Kreidi, Markus S. Schöffler, James R. Harries, Yusuke Tamenori, Yuichiro Morishita, Isao H. Suzuki, Norio Saito, and Kiyoshi Ueda. Probing molecular bond-length using molecular-frame photoelectron angular distributions. *The Journal of Chemical Physics*, 150(17):174306, 2019.
- [26] P. Emma, R. Akre, J. Arthur, R. Bionta, C. Bostedt, J. Bozek, A. Brachmann, P. Bucksbaum, R. Coffee, F.-J. Decker, Y. Ding, D. Dowell, S. Edstrom, A. Fisher, J. Frisch, S. Gilevich, J. Hastings, G. Hays, Ph. Hering, Z. Huang, R. Iverson, H. Loos, M. Messerschmidt, A. Miahnahri, S. Moeller, H.-D. Nuhn, G. Pile, D. Ratner, J. Rzepiela, D. Schultz, T. Smith, P. Stefan, H. Tompkins, J. Turner, J. Welch, W. White, J. Wu, G. Yocky, and J. Galayda. First lasing and operation of an Ångström-wavelength free-electron laser. *Nature Photonics*, 4:641–647, 2010.
- [27] F. Krasniqi, B. Najjari, L. Strüder, D. Rolles, A. Voitkiv, and J. Ullrich. Imaging molecules from within: Ultrafast angström-scale structure determination of molecules via photoelectron holography using free-electron lasers. *Physical Review A*, 81:033411, Mar 2010.
- [28] W. Decking, S. Abeghyan, P. Abramian, A. Abramsky, A. Aguirre, C. Albrecht, P. Alou, M. Altarelli, P. Altmann, K. Amyan, V. Anashin, E. Apostolov, K. Appel, D. Augustine, V. Ayvazyan, S. Baark, F. Babies, N. Baboi, P. Bak, V. Balandin, R. Baldinger, B. Baranasic, S. Barbanotti, O. Belikov, V. Belokurov, L. Belova, V. Belyakov, S. Berry, M. Bertucci, B. Beutner, A. Block, M. Blöcher, T. Böckmann, C. Bohm, M. Böhnert, V. Bondar, E. Bondarchuk, M. Bonezzi, P. Borowiec, C. Bösch, U. Bösenberg, A. Bosotti, R. Böspflug, M. Bousonville, E. Boyd, Y. Bozhko, A. Brand, J. Branlard, S. Briechele, F. Brinker, S. Brinker, R. Brinkmann, S. Brockhauser, O. Brovko, H. Brück, A. Brüdgam, L. Butkowski, T. Büttner, J. Calero, E. Castro-Carballo, G. Cattalanotto, J. Charrier, J. Chen, A. Cherepenko, V. Cheskidov, M. Chiodini, A. Chong, S. Choroba, M. Chorowski, D. Churanov, W. Cichalewski, M. Clausen, W. Clement, C. Cloué, J. A. Cobos, N. Coppola, S. Cunis, K. Czuba, M. Czwalinna, B. D’Almagne, J. Dammann, H. Danared, A. de Zubiaurre Wagner, A. Delfs, T. Delfs, F. Dietrich, T. Dietrich, M. Dohlus, M. Dommach, A. Donat, X. Dong, N. Doynikov, M. Dressel, M. Duda, P. Duda, H. Eckoldt, W. Ehsan, J. Eidam, F. Eints, C. Engling, U. Englisch, A. Ermakov, K. Escherich, J. Eschke, E. Saldin, M. Faesing, A. Fallou, M. Felber, M. Fenner, B. Fernandes, J. M. Fernández, S. Feucker, K. Filippakopoulos, K. Floettmann, V. Fogel, M. Fontaine, A. Francés, I. Freijo Martin, W. Freund, T. Freyermuth, M. Friedland, L. Fröhlich, M. Fusetti, J. Fydrich, A. Gallas, O. García, L. Garcia-Tabares, G. Geloni, N. Gerasimova, C. Gerth, P. Geßler, V. Gharibyan, M. Gloor, J. Głowinkowski, A. Goessel, Z. Gołębiewski, N. Golubeva, W. Grabowski, W. Graeff, A. Grebentsov, M. Grecki, T. Grevsmuehl, M. Gross,

- U. Grosse-Wortmann, J. Grünert, S. Grunewald, P. Grzegory, G. Feng, H. Guler, G. Gusev, J. L. Gutierrez, L. Hagge, M. Hamberg, R. Hanneken, E. Harms, I. Hartl, A. Hauberg, S. Hauf, J. Hauschildt, J. Hauser, J. Havlicek, A. Hedqvist, N. Heidbrook, F. Hellberg, D. Henning, O. Hensler, T. Hermann, A. Hidvégi, M. Hierholzer, H. Hintz, F. Hoffmann, Markus Hoffmann, Matthias Hoffmann, Y. Holler, M. Hüning, A. Ignatenko, M. Ilchen, A. Iluk, J. Iversen, J. Iversen, M. Izquierdo, L. Jachmann, N. Jardon, U. Jastrow, K. Jensch, J. Jensen, M. Ježabek, M. Jidda, H. Jin, N. Johansson, R. Jonas, W. Kaabi, D. Kaefer, R. Kammering, H. Kapitzka, S. Karabekyan, S. Karstensen, K. Kasprzak, V. Katalev, D. Keese, B. Keil, M. Kholopov, M. Killenberger, B. Kitaev, Y. Klimchenko, R. Klos, L. Knebel, A. Koch, M. Koepke, S. Köhler, W. Köhler, N. Kohlstrunk, Z. Konopkova, A. Konstantinov, W. Kook, W. Koprek, M. Körfer, O. Korth, A. Kosarev, K. Kosiński, D. Kostin, Y. Kot, A. Kotarba, T. Kozak, V. Kozak, R. Kramert, M. Krasilnikov, A. Krasnov, B. Krause, L. Kravchuk, O. Krebs, R. Kretschmer, J. Kreutzkamp, O. Kröplin, K. Krzysik, G. Kube, H. Kuehn, N. Kujala, V. Kulikov, V. Kuzminych, D. La Civita, M. Lacroix, T. Lamb, A. Lancetov, M. Larsson, D. Le Pinvidic, S. Lederer, T. Lensch, D. Lenz, A. Leuschner, F. Levenhagen, Y. Li, J. Liebing, L. Lilje, T. Limberg, D. Lipka, B. List, J. Liu, S. Liu, B. Lorbeer, J. Lorkiewicz, H. H. Lu, F. Ludwig, K. Machau, W. Maciocha, C. Madec, C. Magueur, C. Maiano, I. Maksimova, K. Malcher, T. Maltezopoulos, E. Mamoshkina, B. Manschwetus, F. Marcellini, G. Marinkovic, T. Martinez, H. Martirosyan, W. Maschmann, M. Maslov, A. Matheisen, U. Mavric, J. Meißner, K. Meissner, M. Messerschmidt, N. Meyners, G. Michalski, P. Michelato, N. Mildner, M. Moe, F. Moglia, C. Mohr, S. Mohr, W. Möller, M. Mommerz, L. Monaco, C. Montiel, M. Moretti, I. Morozov, P. Morozov, D. Mross, J. Mueller, C. Müller, J. Müller, K. Müller, J. Munilla, A. Münnich, V. Muratov, O. Napoly, B. Näser, N. Nefedov, Reinhard Neumann, Rudolf Neumann, N. Ngada, D. Noelle, F. Obier, I. Okunev, J. A. Oliver, M. Omet, A. Oppelt, A. Ottmar, M. Oublaïd, C. Pagani, R. Papparella, V. Paramonov, C. Peitzmann, J. Penning, A. Perus, F. Peters, B. Petersen, A. Petrov, I. Petrov, S. Pfeiffer, J. Pflüger, S. Philipp, Y. Pienaud, P. Pierini, S. Pivovarov, M. Planas, E. Plawski, M. Pohl, J. Polinski, V. Popov, S. Prat, J. Prenting, G. Priebe, H. Prysichelski, K. Przygoda, E. Pyata, B. Racky, A. Rathjen, W. Ratuschni, S. Regnaud-Campderros, K. Rehlich, D. Reschke, C. Robson, J. Roeber, M. Roggli, J. Rothenburg, E. Rusiński, R. Rybaniec, H. Sahling, M. Salmani, L. Samoylova, D. Sanzone, F. Saretzki, O. Sawlanski, J. Schaffran, H. Schlarb, M. Schlösser, V. Schlott, C. Schmidt, F. Schmidt-Foehre, M. Schmitz, M. Schmökel, T. Schnautz, E. Schneidmiller, M. Scholz, B. Schöneburg, J. Schultze, C. Schulz, A. Schwarz, J. Sekutowicz, D. Sellmann, E. Semenov, S. Serkez, D. Sertore, N. Shehzad, P. Shemarykin, L. Shi, M. Sienkiewicz, D. Sikora, M. Sikorski, A. Silenzi, C. Simon, W. Singer, X. Singer, H. Sinn, K. Sinram, N. Skvorodnev, P. Smirnow, T. Sommer, A. Sorokin, M. Stadler, M. Steckel, B. Steffen, N. Steinhau-Kühl, F. Stephan, M. Stodulski, M. Stolper, A. Sulimov, R. Susen, J. Świerblewski, C. Sydlo, E. Syresin, V. Sytchev, J. Szuba, N. Tesch, J. Thie, A. Thiebault, K. Tiedtke, D. Tischhauser, J. Tolkiehn, S. Tomin, F. Tonisch, F. Toral, I. Torbin, A. Trapp, D. Treyer, G. Trowitzsch, T. Trublet, T. Tschentscher, F. Ullrich, M. Vannoni, P. Varela, G. Varghese, G. Vashchenko, M. Vasic, C. Vazquez-Velez, A. Verguet, S. Vilcins-Czvitkovits, R. Vilanueva, B. Visentin, M. Viti, E. Vogel, E. Volobuev, R. Wagner, N. Walker, T. Wamsat, H. Weddig, G. Weichert, H. Weise, R. Wenndorf, M. Werner, R. Wichmann, C. Wiebers, M. Wiencek, T. Wilksen, I. Will, L. Winkelmann, M. Winkowski, K. Wittenburg, A. Witzig, P. Wlk, T. Wohlenberg, M. Wojciechowski, F. Wolff-Fabris, G. Wrochna, K. Wrona, M. Yakopov, B. Yang, F. Yang, M. Yurkov, I. Zagorodnov, P. Zalden, A. Zavadtsev, D. Zavadtsev, A. Zhirnov, A. Zhukov, V. Ziemann, A. Zolotov, N. Zolotukhina, F. Zummack, and D. Zybin. A MHz-repetition-rate hard X-ray free-electron laser driven by a superconducting linear accelerator. *Nature Photonics*, 14(6):391–397, May 2020.
- [29] Gregor Kastirke, Markus S. Schöffler, Miriam Weller, Jonas Rist, Rebecca Boll, Nils Anders, Thomas M. Baumann, Sebastian Eckart, Benjamin Erk, Alberto De Fanis, Kilian Fehre, Averell Gattou, Sven Grundmann, Patrik Grychtol, Alexander Hartung, Max Hofmann, Markus Ilchen, Christian Janke, Max Kircher, Maksim Kunitski, Xiang Li, Tommaso Mazza, Niklas Melzer, Jacobo Montano, Valerija Music, Giammarco Nalin, Yevheniy Ovcharenko, Andreas Pier, Nils Rennhack, Daniel E. Rivas, Reinhard Dörner, Daniel Rolles, Artem Rudenko, Philipp Schmidt, Juliane Siebert, Nico Strenger, Daniel Trabert, Isabel Vela-Perez, Rene Wagner, Thorsten Weber, Joshua B. Williams, Pawel Ziolkowski, Lothar Ph. H. Schmidt, Achim Czasch, Florian Trinter, Michael Meyer, Kiyoshi Ueda, Philipp V. Demekhin, and Till Jahnke. Photoelectron Diffraction Imaging of a Molecular Breakup Using an X-Ray Free-Electron Laser. *Physical Review X*, 10:021052, Jun 2020.
- [30] F.A. Gianturco and A. Jain. The theory of electron scattering from polyatomic molecules. *Physics Reports*, 143(6):347–425, 1986.
- [31] C. Brouder, M. F. Ruiz López, R. F. Pettifer, M. Benfatto, and C. R. Natoli. Systematic approach to the calculation of the polarization-dependent (and polarization-averaged) general term of the curved-wave multiple-scattering series in the x-ray-absorption cross section. *Physical Review B*, 39:1488–1500, Jan 1989.
- [32] A R Williams and J van W Morgan. Multiple scattering by non-muffin-tin potentials: general formulation. *Journal of Physics C: Solid State Physics*, 7(1):37–60, jan 1974.
- [33] C. R. Natoli, M. Benfatto, S. Della Longa, and K. Hatada. X-ray absorption spectroscopy: state-of-the-art analysis. *Journal of Synchrotron Radiation*, 10(1):26–42, Jan 2003.
- [34] A. Gonis and W. H. Butler. *Multiple Scattering in Solids*. Springer-Verlag New York, 2000.
- [35] D A Varshalovich, A N Moskalev, and V K Khersonskii. *Quantum Theory of Angular Momentum*. WORLD SCIENTIFIC, 1988.
- [36] J. A. Kelber, D. R. Jennison, and R. R. Rye. Analysis of the Auger spectra of CO and CO₂. *The Journal of Chemical Physics*, 75(2):652–662, 1981.
- [37] V. Feyer, P. Bolognesi, M. Coreno, K. C. Prince, L. Avaldi, L. Storchi, and F. Tarantelli. Effects of nuclear dynamics in the low-kinetic-energy Auger spectra of CO and CO₂. *The Journal of Chemical Physics*, 123(22):224306, 2005.
- [38] L. S. Cederbaum, P. Campos, F. Tarantelli, and A. Sgamellotti. Band shape and vibrational structure in Auger spectra: Theory and application to carbon monoxide. *The Journal of Chemical Physics*, 95(9):6634–6644, 1991.
- [39] Francesco Aquilante, Jochen Autschbach, Rebecca K. Carlson, Liviu F. Chibotaru, Mickaël G. Delcey, Luca De Vico, Ignacio Fdez. Galván, Nicolas Ferré, Luis Manuel Frutos, Laura Gagliardi, Marco Garavelli, Angelo Giussani, Chad E. Hoyer, Giovanni Li Manni, Hans Lischka, Dongxia Ma, Per Åke Malmqvist, Thomas Müller, Artur Nenov, Massimo Olivucci, Thomas Bondo Pedersen, Daoling Peng, Felix Plasser, Ben Pritchard, Markus Reiher, Ivan Rivalta, Igor Schapiro, Javier Segarra-Martí, Michael Stenrup, Donald G. Truhlar, Liviu Ungur, Alessio Valentini, Steven Vancoillie, Valera Veryazov, Victor P. Vysotskiy, Oliver Weingart, Felipe Zapata, and Roland Lindh. Molcas 8: New capabilities for multiconfigurational quantum chemical calculations across the periodic table. *Journal of Computational Chemistry*, 37(5):506–541, 2016.
- [40] Per Åke Malmqvist, Kristine Pierloot, Abdul Rehman Moughal Shahi, Christopher J. Cramer, and Laura Gagliardi. The restricted active space followed by second-order perturbation theory method: Theory and application to the study of CuO₂ and Cu₂O₂ systems. *The Journal of Chemical Physics*, 128(20):204109, 2008.
- [41] Vicenta Sauri, Luis Serrano-Andrés, Abdul Rehman Moughal Shahi, Laura Gagliardi, Steven Vancoillie, and Kristine Pierloot. Multiconfigurational Second-Order Perturbation Theory

- Restricted Active Space (RASPT2) Method for Electronic Excited States: A Benchmark Study. Journal of Chemical Theory and Computation, 7(1):153–168, 2011. PMID: 26606229.
- [42] Giovanni Ghigo, Björn O. Roos, and Per Åke Malmqvist. A modified definition of the zeroth-order Hamiltonian in multiconfigurational perturbation theory (CASPT2). Chemical Physics Letters, 396(1):142–149, 2004.
- [43] Per Aake. Malmqvist, Alistair. Rendell, and Bjoern O. Roos. The restricted active space self-consistent-field method, implemented with a split graph unitary group approach. The Journal of Physical Chemistry, 94(14):5477–5482, 1990.
- [44] Björn O. Roos, Roland Lindh, Per-åke Malmqvist, Valera Veryazov, and Per-Olof Widmark. Main Group Atoms and Dimers Studied with a New Relativistic ANO Basis Set. The Journal of Physical Chemistry A, 108(15):2851–2858, 2004.
- [45] Daoling Peng and Markus Reiher. Exact decoupling of the relativistic Fock operator. Theoretical Chemistry Accounts, 131:1081, 2012.
- [46] Bernd A. Heß, Christel M. Marian, Ulf Wahlgren, and Odd Gropen. A mean-field spin-orbit method applicable to correlated wavefunctions. Chemical Physics Letters, 251(5):365–371, 1996.
- [47] Didier Sébilleau, Calogero Natoli, George M. Gavaza, Haifeng Zhao, Fabiana Da Pieve, and Keisuke Hatada. MsSpec-1.0: A multiple scattering package for electron spectroscopies in material science. Computer Physics Communications, 182(12):2567–2579, 2011.
- [48] Misato Kazama, Hiroshi Shinotsuka, Takashi Fujikawa, Mauro Stener, Piero Decleva, Jun ichi Adachi, Tomoya Mizuno, and Akira Yagishita. Multiple-scattering calculations for 1s photoelectron angular distributions from single oriented molecules in the energy region above 50eV. Journal of Electron Spectroscopy and Related Phenomena, 185(11):535–545, 2012.
- [49] L. Hedin and S. Lundqvist. Effects of Electron-Electron and Electron-Phonon Interactions on the One-Electron State of Solids. In F. Seitz, D. Turnbull, and H. Ehrenreich, editors, Solid State Physics, volume 23, pages 1–517. Academic Press, New York, 1969.
- [50] L. Hedin and B I Lundqvist. Explicit local exchange-correlation potentials. Journal of Physics C: Solid State Physics, 4(14):2064–2083, oct 1971.
- [51] J.P. Desclaux. A multiconfiguration relativistic DIRAC-FOCK program. Computer Physics Communications, 9(1):31–45, 1975.
- [52] Trygve Helgaker, Poul Jorgensen, and Jeppe Olsen. Molecular Electronic-Structure Theory. Wiley, 2000.
- [53] S. F. Boys and Alfred Charles Egerton. Electronic wave functions - I. A general method of calculation for the stationary states of any molecular system. Proceedings of the Royal Society of London. Series A. Mathematical and Physical Sciences, 200(1063):542–554, 1950.
- [54] Naoki Komiya, Fukiko Ota, Junqing Xu, and Keisuke Hatada. ES2MS: Interface from Electronic Structure Codes to Multiple Scattering Codes. In Didier Sébilleau, Keisuke Hatada, and Hubert Ebert, editors, Multiple Scattering Theory for Spectroscopies, pages 275–282. Springer International Publishing, Cham, 2018.
- [55] Joe G. Norman Jr. Non-empirical versus empirical choices for overlapping-sphere radii ratios in SCF-X_α-SW calculations on ClO₄⁻ and SO₂. Molecular Physics, 31(4):1191–1198, 1976.
- [56] Frank Herman, Arthur R. Williams, and Keith H. Johnson. Multiple scattering method based on overlapping atomic spheres with application to the TCNQ molecule. The Journal of Chemical Physics, 61(9):3508–3522, 1974.
- [57] I. Turek, V. Drchal, J. Kudrnovsky, M. Sob, and P. Weinberger. Electronic Structure of Disordered Alloys, Surfaces and Interfaces. Springer US, 1997.
- [58] J. J. Rehr, R. C. Albers, C. R. Natoli, and E. A. Stern. New high-energy approximation for x-ray-absorption near-edge structure. Physical Review B, 34:4350–4353, Sep 1986.
- [59] F. Ota, K. Hatada, D. Sébilleau, K. Ueda, and K. Yamazaki. Theory on polarization-averaged core-level molecular-frame photoelectron angular distributions: II. Extracting the X-ray induced fragmentation dynamics of carbon monoxide dication from forward and backward intensities. To be published in J. Phys. B: At. Mol. Opt. (this volume as Paper II).
- [60] Qiqi Zhang, Shinichi Fukahori, Toshiaki Ando, Reika Kanya, Atsushi Iwasaki, Tim Rathje, Gerhard G. Paulus, and Kaoru Yamanouchi. Absolute carrier-envelope-phase dependences of single and double ionization of methanol in a near-IR few-cycle laser field. The Journal of Chemical Physics, 152(19):194304, 2020.
- [61] Nagitha Ekanayake, Muath Nairat, Balram Kaderiya, Peyman Feizollah, Bethany Jochim, Travis Severt, Ben Berry, Kanaka Raju Pandiri, Kevin D. Carnes, Shashank Pathak, Daniel Rolles, Artem Rudenko, Itzik Ben-Itzhak, Christopher A. Mancuso, B. Scott Fales, James E. Jackson, Benjamin G. Levine, and Marcos Dantus. Mechanisms and time-resolved dynamics for trihydrogen cation (H₃⁺) formation from organic molecules in strong laser fields. Scientific Reports, 7(1):4703, Jul 2017.
- [62] Li Fang, Hui Xiong, Edwin Kukk, Vladmire S. Petrovic, and Nora Berrah. X-ray-initiated photodissociation of the glycine molecule. Phys. Rev. A, 98:053408, Nov 2018.
- [63] Eero Itälä, Helena Levola, Dang Trinh Ha, Kuno Kooser, Elisabeth Rachlew, and Edwin Kukk. Photofragmentation of Serine Following C 1s Core Ionization—Comparison with Cysteine. The Journal of Physical Chemistry A, 120(28):5419–5426, Jul 2016.
- [64] Dang Trinh Ha, Y. Wang, M. Alcamí, E. Itälä, K. Kooser, S. Urpelainen, M. A. Huels, E. Kukk, and F. Martín. Fragmentation Dynamics of Doubly Charged Methionine in the Gas Phase. The Journal of Physical Chemistry A, 118(8):1374–1383, Feb 2014.
- [65] D. T. Ha, K. Yamazaki, Y. Wang, M. Alcamí, S. Maeda, H. Kono, F. Martín, and E. Kukk. Fragmentation network of doubly charged methionine: Interpretation using graph theory. The Journal of Chemical Physics, 145(9):094302, 2016.
- [66] Raúl Montero, Álvaro Peralta Conde, Virginia Ovejas, Marta Fernández-Fernández, Fernando Castaño, Javier R. Vázquez de Aldana, and Asier Longarte. Femtosecond evolution of the pyrrole molecule excited in the near part of its UV spectrum. The Journal of Chemical Physics, 137(6):064317, 2012.
- [67] Kaoru Yamazaki, Takashi Nakamura, Naoyuki Niitsu, Manabu Kanno, Kiyoshi Ueda, and Hirohiko Kono. Communication: Two-step explosion processes of highly charged fullerene cations C₆₀^{q+} (q = 20–60). The Journal of Chemical Physics, 141(12):121105, 2014.
- [68] Kaoru Yamazaki, Naoyuki Niitsu, Manabu Kanno, Kiyoshi Ueda, and Hirohiko Kono. Capturing the photo-induced dynamics of nano-molecules by X-ray free electron laser induced Coulomb explosion. The Journal of Chemical Physics, 151(12):124305, 2019.
- [69] K. Nagaya, K. Motomura, E. Kukk, Y. Takahashi, K. Yamazaki, S. Ohmura, H. Fukuzawa, S. Wada, S. Mondal, T. Tachibana, Y. Ito, R. Koga, T. Sakai, K. Matsunami, K. Nakamura, M. Kanno, A. Rudenko, C. Nicolas, X.-J. Liu, C. Miron, Y. Zhang, Y. Jiang, J. Chen, M. Anand, D. E. Kim, K. Tono, M. Yabashi, M. Yao, H. Kono, and K. Ueda. Femtosecond charge and molecular dynamics of I-containing organic molecules induced by intense X-ray free-electron laser pulses. Faraday Discuss., 194:537–562, 2016.
- [70] E. Kukk, D. T. Ha, Y. Wang, D. G. Piekarski, S. Diaz-Tendero, K. Kooser, E. Itälä, H. Levola, M. Alcamí, E. Rachlew, and F. Martín. Internal energy dependence in x-ray-induced molecular fragmentation: An experimental and theoretical study of thiophene. Phys. Rev. A, 91:043417, Apr 2015.
- [71] Ludger Inhester, Bart Oostenrijk, Minna Patanen, Esko Kokkonen, Stephen H. Southworth, Christoph Bostedt, Oksana Travnikova, Tatiana Marchenko, Sang-Kil Son, Robin Santra, Marc Simon, Linda Young, and Stacey L. Sorensen. Chemical Understanding of the Limited Site-Specificity in Molecular Inner-Shell

- Photofragmentation. The Journal of Physical Chemistry Letters, 9(5):1156–1163, Mar 2018.
- [72] A. Rudenko, L. Inhester, K. Hanasaki, X. Li, S. J. Robotjazi, B. Erk, R. Boll, K. Toyota, Y. Hao, O. Vendrell, C. Bomme, E. Savelyev, B. Rudek, L. Foucar, S. H. Southworth, C. S. Lehmann, B. Kraessig, T. Marchenko, M. Simon, K. Ueda, K. R. Ferguson, M. Bucher, T. Gorkhover, S. Carron, R. Alonso-Mori, J. E. Koglin, J. Correa, G. J. Williams, S. Boutet, L. Young, C. Bostedt, S.-K. Son, R. Santra, and D. Rolles. Femtosecond response of polyatomic molecules to ultra-intense hard X-rays. Nature, 546(7656):129–132, Jun 2017.
- [73] Martin Richter, Philipp Marquetand, Jesús González-Vázquez, Ignacio Sola, and Leticia González. SHARC: ab initio molecular dynamics with surface hopping in the adiabatic representation including arbitrary couplings. J. Chem. Theory Comput., 7(5):1253–1258, 2011.
- [74] Sebastian Mai, Philipp Marquetand, and Leticia González. Nonadiabatic Dynamics: The SHARC Approach. WIREs Comput. Mol. Sci., 8:e1370, 2018.
- [75] Mario Barbatti, Matthias Ruckebauer, Felix Plasser, Jiri Pittner, Giovanni Granucci, Maurizio Persico, and Hans Lischka. Newton-X: a surface-hopping program for nonadiabatic molecular dynamics. WIREs Computational Molecular Science, 4(1):26–33, 2014.
- [76] Weijie Hua, Shaul Mukamel, and Yi Luo. Transient X-ray Absorption Spectral Fingerprints of the S_1 Dark State in Uracil. The Journal of Physical Chemistry Letters, 10(22):7172–7178, Nov 2019.
- [77] Motomichi Tashiro, Kiyoshi Ueda, and Masahiro Ehara. Auger decay of molecular double core-hole state. The Journal of Chemical Physics, 135(15):154307, 2011.
- [78] Masaki Mitani, Osamu Takahashi, Ko Saito, and Suehiro Iwata. Theoretical molecular Auger spectra with electron population analysis. Journal of Electron Spectroscopy and Related Phenomena, 128(2):103 – 117, 2003.
- [79] Khadijeh Khalili, Ludger Inhester, Caroline Arnold, Anders S. Gertsen, Jens Wenzel Andreasen, and Robin Santra. Simulation of time-resolved x-ray absorption spectroscopy of ultrafast dynamics in particle-hole-excited 4-(2-thienyl)-2,1,3-benzothiadiazole. Structural Dynamics, 7(4):044101, 2020.
- [80] Uriel N. Morzan, Pablo E. Videla, Micheline B. Soley, Erik T. J. Nibbering, and Victor S. Batista. Vibronic Dynamics of Photodissociating ICN from Simulations of Ultrafast X-Ray Absorption Spectroscopy. Angewandte Chemie International Edition, 59(45):20044–20048, 2020.
- [81] Christopher Ehlert and Tillmann Klamroth. PSIXAS: A Psi4 plugin for efficient simulations of X-ray absorption spectra based on the transition-potential and Δ -Kohn-Sham method. Journal of Computational Chemistry, 41(19):1781–1789, 2020.
- [82] C. R. Natoli, M. Benfatto, and S. Doniach. Use of general potentials in multiple-scattering theory. Physical Review A, 34:4682–4694, Dec 1986.